**ISCI, Volume *16***

## Supplemental Information

# Molybdenum Nitride Nanocrystals Anchored on Phosphorus-Incorporated Carbon Fabric as a Negative Electrode for High-Performance Asymmetric Pseudocapacitor

**Deepak P. Dubal, Safwat Abdel-Azeim, Nilesh R. Chodankar, and Young-Kyu Han**

# Transparent Methods

## Chemicals

The phosphomolybdic acid ($H_3PMo_{12}O_{40}.3H_2O$ Kegging type, $PMo_{12}$), hydrochloric acid (HCl), acetone ($C_3H_6O$), ethanol ($C_2H_6O$), hydrogen peroxide ($H_2O_2$) and Ruthenium (III) chloride ($RuCl_3 \cdot xH_2O$), polyvinyl alcohol (PVA) was purchased from sigma Aldrich. The carbon fabric (W0S1002 Carbon Cloth Substrate with thickness 360 μm) was purchased from FC Internationals, South Korea. All regents were used as received without further purification. All the precursor solutions were prepared by using the MilliQ water.

## Design and synthesis of MoN@P-CF

Prior to the deposition, the commercial CF was cleaned with acetone, ethanol and deionized (DI) water using ultrasonic bath (20 min each) and dried in the oven at temperature 80 °C for 24 hr. Initially, well-cleaned CF was immersed in 10 mM phosphomolybdic acid ($H_3PMo_{12}O_{40}.3H_2O$, $PMo_{12}$) solution and sonicated for 30 min. Later, the precursor solution with CF was transferred to Teflon-linked stainless steel autoclave and treated at 120°C for 12 h to achieve $PMo_{12}$ nanoclusters decorated CF. The $PMo_{12}$@CF sample was cleaned with MilliQ water and dried in vacuum oven at 70 °C for 12 hr. Finally, the as-prepared $PMo_{12}$@CF were annealed in tube furnace under ammonia gas flow with a temperature rate of 3 $^oC$/min at three different temperatures 700 °C, 800 °C and 900 °C for 5 hours. The prepared samples were denoted as MoN@P-CF-700, MoN@P-CF-800 and MoN@P-CF-900. All the samples were preserved in vacuum sealed desiccator to avoid the oxidation.

## Synthesis of $RuO_2$ on carbon fabric (CF)

This is the first report on the synthesis of $RuO_2$ on CF by Layer-by-Layer (LBL) deposition method. This is very simple, cost-effective and large scale deposition method. For the deposition of $RuO_2$ on CF, 10 mM $RuCl_3$ was used as the cationic precursor while MilliQ water with 3-4 drops of $H_2O_2$ maintained at 80 °C was utilized as anionic precursor solution. Pre-cleaned CF substrate was immersed in a cationic solution ($RuCl_3$) for 20 sec where the ruthenium species adsorbed on to the CF surface. The CF-substrate was rinsed in MilliQ water for 5 sec to remove loosely bound Ru species. Later, Ru-species@CF substrate was immersed in anionic solution (kept at 80 °C) for 20 sec to form a layer of hydrous ruthenium oxide material. Finally, the CF-substrate was again rinsed for 5 sec to remove excess or unreacted species. We have performed 120 deposition cycles to get a terminal thickness where the mass loading was determined to be 0.9 mg/cm$^2$. After complete reaction cycles, the $RuO_2$@CF samples were cleaned with water and dried in vacuum oven for 12 hr at 70 °C.

**Materials characterizations**

All the samples were characterized by using different characterizations techniques. The structural analysis was performed by Powder X-ray diffraction patterns using X-ray Powder Diffractometer (Rigaku MiniFlex600) (Cu Kα radiation and PIXel detector). The compositional information as collected using Raman spectra, which was recorded using Raman Spectrometer (Horiba Scientific). The oxidation states and surface composition various elements in the sample was measured using X-ray photoelectron spectroscopy XPS (ESCALAB-MKII). The surface morphological analysis were performed using series of characterization techniques such as field-emission scanning electron microscopy, FE-SEM (FEI Quanta 450 FEG Environmental SEM) and transmission electron microscopy, TEM (FEI Titan Themis 80-200). The energy-dispersive X-ray spectroscopy (EDS) analyzer attached to the FE-SEM was used to investigate the elemental composition.

**Assembly of solid-state all pseudo-capacitive MoN@P-CF//$RuO_2$@CF asymmetric cell**

Prior to assemble a full cell, MoN@P-CF and $RuO_2$@CF electrodes were tested in 1 M $H_2SO_4$ using 3-electrode configuration. In order to approach the highest cell voltage, the charges stored in positive and negative electrodes must be balanced by adjusting the mass loading of each of the active electrode materials. The capacitance of the MoN@P-CF (negative electrode) and $RuO_2$@CF (positive electrode) were balanced to satisfy $Q_+ = Q_-$.

$$\frac{m_{MoN}}{m_{RuO2}} = \frac{C_{RuO2} \times E_{RuO2}}{C_{MoN} \times E_{MoN}} = \frac{2}{1} \qquad (1)$$

The mass ratio of MoN@P-CF:$RuO_2$@CF was maintained to ~ 1:2. Thus, the total mass loading of active material in both electrodes was 3.4 mg/cm$^2$. The $W_2N$@P-CF//PPy@CF asymmetric device was assembled in coin cell design with 1 M $H_2SO_4$ electrolyte and a glass fiber separator.

The asymmetric cell was fabricated using MoN@P-CF as a negative electrode, $RuO_2$@CF as a positive electrode with PVA-$H_2SO_4$ gel as electrolyte and separator. PVA-$H_2SO_4$ gel-electrolyte was prepared by dissolving 3 g of PVA in 30 mL of deionized water at 70 °C under vigorous stirring for 60 min. After cooling down, 3 g of $H_2SO_4$ was added in the PVA solution and vigorously stirred for next 30 min to form a polymer gel-electrolyte. Now, both MoN@P-CF and $RuO_2$@CF electrodes were soaked in gel-electrolyte for 2 min and then dried at room temperature for 12 h to form a thin layer of the gel electrolyte on both the electrode. Finally, both the electrodes were pressed on each other to form flexible all pseudocapacitive solid-state MoN@P-CF and $RuO_2$@CF asymmetric cell.

**Electrochemical Measurements**

The electrochemical performances of individual electrodes and final asymmetric cells such as cyclic voltammetry (CV), galvanostatic charge/discharge (GCD) and electrochemical impedance (EIS) were conducted using a CHI760D electrochemical workstation. For three-electrode measurements, MoN@P-CF and $RuO_2$@CF electrodes were used as the working electrodes with platinum wire and Ag/AgCl as the counter and reference electrodes, respectively.

*Calculations*: Gravimetric (F/g) and areal specific capacitance (mF/cm$^2$) of electrode materials was calculated from the CD curves by integrating the discharge portion using the following equation:

$$C_s = \frac{I \times \Delta t}{m \times V} \; OR \quad C_A = \frac{I \times \Delta t}{A \times V} \qquad (2)$$

where *I* is the current (mA), *V* is the potential window (V) and *m* is the mass of the active material (mg).

*Two-electrode configuration (cell measurements)*

The areal ($C_A$) and volumetric ($C_V$) capacitance were estimated from the slope of the discharge curve using the following equations:

$$C_A = \frac{I \int V dt}{Area \times V^2} \quad OR \; C_A = \frac{I \int V dt}{Volume \times V^2} \qquad (3)$$

Where $C_A$ and $C_V$ are areal and volumetric capacitances, respectively. *I* is the applied current, *Δt* is the discharging time, *V* (V) is the voltage window, Volume (cm$^3$) of the whole device (The area and thickness of our asymmetric cells is about 0.785 cm$^2$ (Area, A=πr$^2$, 3.14 × (0.5)$^2$) and 0.088 cm. Hence, the whole volume of device is about 0.069 cm$^3$, *ΔV* (V) is the voltage window. It is worth mentioning that the volumetric capacitances were calculated taking into account the volume of the device stack. This includes the active material, the flexible substrate and the separator with electrolyte.

Volumetric energy (E, Wh/cm$^3$) and power density (P, W/cm$^3$) of the devices were obtained from the following equations:

$$E = \frac{1}{2 \times 3600} C_V \Delta V^2 \qquad (4)$$

$$P = \frac{3600 \times E}{\Delta t} \qquad (5)$$

where *E* (Wh/cm$^3$) is the energy density, $C_V$ is the volumetric capacitance obtained from Equation (4) and *ΔV* (V) is the voltage window, P (W/cm$^3$) is the power density.

*Electrochemical Impedance Calculations:*

Furthermore, the capacitive behavior of device can also be evaluated from EIS technique by calculating the real and imaginary capacitance at a corresponding frequency using following equations:

$$C(\omega) = C^{'}(\omega) - jC^{''}(\omega) \quad (6)$$

Where,

$$C^{'}(\omega) = \frac{Z^{''}(\omega)}{\omega \mid Z(\omega) \mid^2} \quad (7)$$

$$C^{''}(\omega) = \frac{Z^{'}(\omega)}{\omega \mid Z(\omega) \mid^2} \quad (8)$$

where '*Z'* the complex impedance represented as $Z(\omega) = Z'(\omega) + Z''(\omega)$ and $\omega = 2\pi f$ where *f* is the frequency. $C'(\omega)$ is the real accessible capacitance of the electrode while $C''(\omega)$ is the energy loss due to the irreversible processes of the electrodes, $Z'$ and $Z''$ are the real and imaginary parts of the Nyquist plot, respectively.

**Density Functional Theory (DFT) computational details and models**

All Density functional theory (DFT) simulations were carried out using the Vienna ab initio simulation package (VASP) (Kresse et al. 1993; Kresse et al. 1994) with the projector augmented wave pseudopotentials (PAW) (Blochl, 1994) and the periodic boundary conditions. The brillouin zone was sampled using 3 x 3 x 1 a Monkhorst-pack (Monkhorst and Pack, 1976) gamma centered mesh, and Gaussian smearing of 0.015 eV was used for the occupations of the electronic levels. Perdew-Burke-Ernzerhof (PBE) (Perdew et al. 1996; Perdew et al. 1997) functional within the generalized gradient approximation (GGA), was used to describe the electron interaction energy of exchange correlation. The electronic energies were converged within the limit of 10−7 ev and a cutoff of 600 ev was used. All geometries were optimized using 0.01 eV/Å force criteria. All the calculations were spin polarized. $H3O^+$ molecules were used to carry out all the proton adsorption calculations for CF, P-CF, MoN and their interfaces. The adsorption energy of proton within the supercells was calculated as follows:

$$E_{S@H3O} = E_{S@H3O} - [E_S + E_{H3O+}]$$

Where $E_{S@H3O}$ is the total energy of the substrate (Cf, P-CF, MoN@CF, MoN@P-CF) with the adsorbed $H_3O^+$, $E_S$ is the total energy of a clean slab, and $E_{H3O}$ is the energy of the hydronium cation. Through all the calculations, DFT+D3 approach developed by Grimme, was used for the long-range dispersion correction (Grimme et al. 2010).

For graphene fiber (CF) model, we have adopted 7 x 7 supercell (98 C atoms) and doped it with one and two phosphorus atoms which are corresponding to 1.0 at% and 2.0 at% of P:C, the latter is the

experimental atomic ratio (2.1 at%). We decide to use very large graphene layer and large vacuum distance of 20 Å in order to minimize the charge-image interactions. We have adopted P-sp3 type in our calculation because it reported as the most stable configuration of P-doped graphene system (P-CF) (Yang et al. 2017).

For MoN nanoparticles, we have modeled it using a 2 x 2 x 1 (100) slab of the hexagonal MoN (128 atoms) (Bull et al. 2004) and a thickness of 8 layer. Four of them were frozen and the upper four layers were relaxed. GGA+U formalism was used to describe the strong on-site coulomb interactions; we have adopted Dudraev et. al approach (Dudraev et al. 1998) which involves one parameter called the effective U (U-J, where U is the on-site coulomb repulsion and J is the on-site Hund exchange coupling. The U parameter was set to 3.0 ev in all our simulations involved MoN and the anti-ferromagnetic state used to describe the magnetism of the slab. The interfaces of MoN@CF and MoN@P-CF were generated using 6 x 6 x 1 of graphene sheet (CF, 72 atoms) and the above mentioned MoN slab. Here, we kept the doping ratio 1.4 at % for P-CF (which very near from of the experimental ratio 2.1 at%) to minimize the computational cost. The binding charge density was calculated using VESTA (Momma et al. 2011). Atom In Molecules (AIM) approach was used for the atomic charge analysis using bader code developed by henkelman group (Yu et al. 2011).

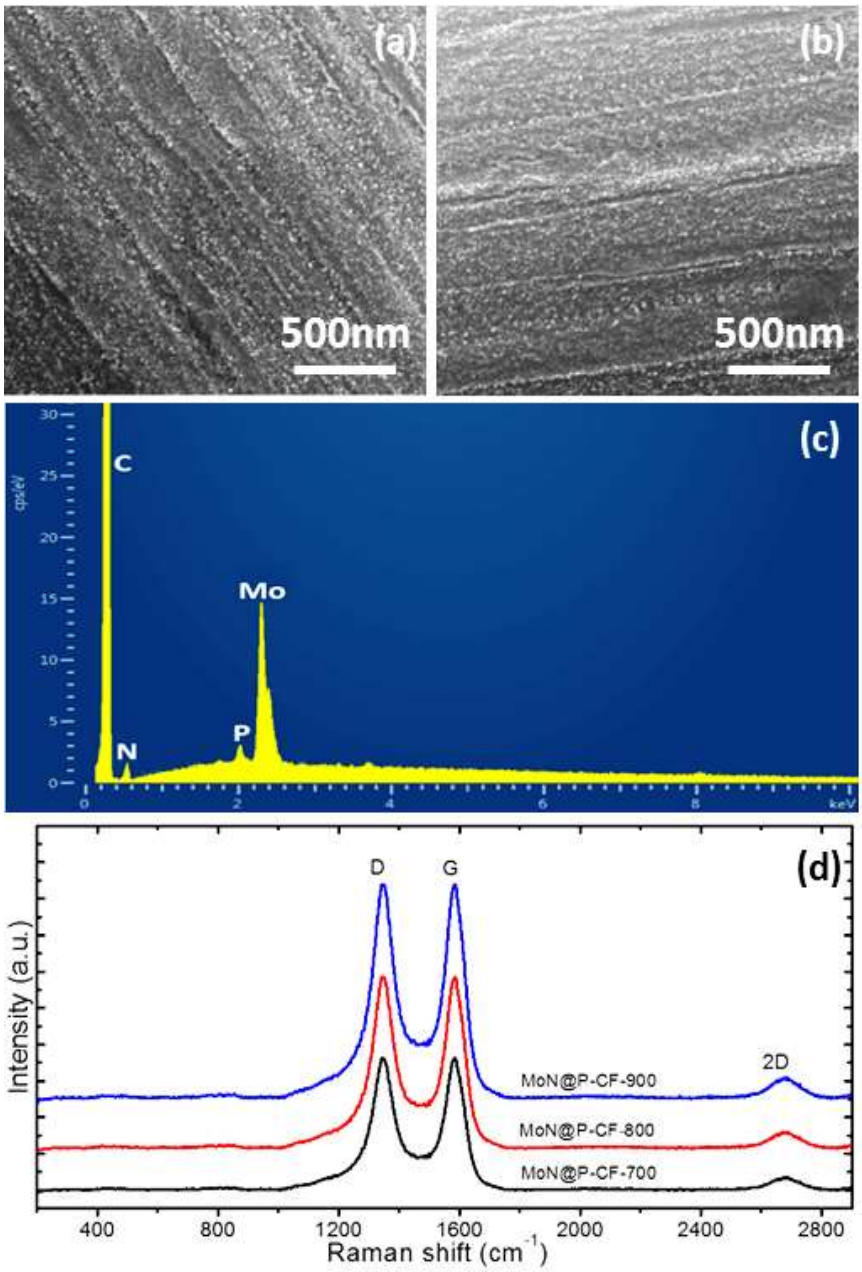


**Figure S1 Characterizations of MoN@P-CF samples, Related to Figure 2.** (a, b) SEM images of MoN@P-CF-700 and MoN@P-CF-800 samples, respectively. (c) EDAX pattern of MoN@P-CF-900 electrode, confirming the presence of Mo, N, C and P. (d) and (b) Raman spectra for MoN@P-CF samples prepared at different nitridation temperatures.

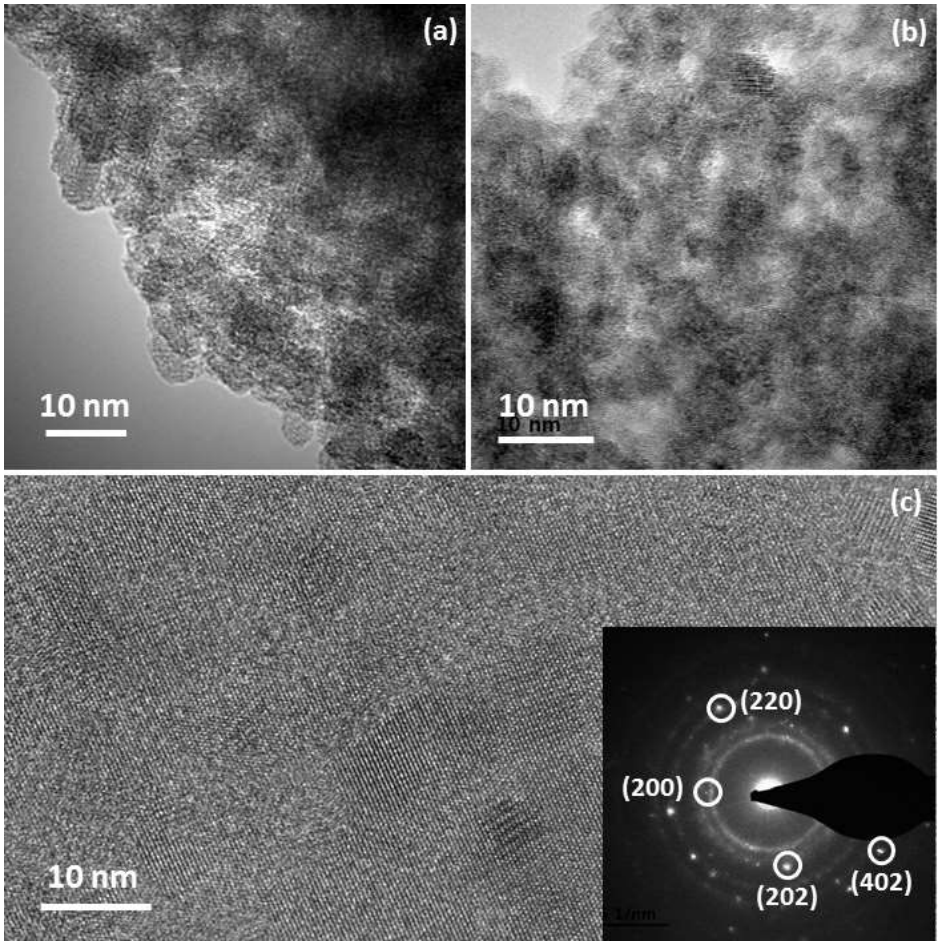


**Figure S2 Characterizations of MoN@P-CF samples, Related to Figure 2.** (a, b) TEM images for the MoN@P-CF sample prepared at 900 C, implying the formation of ultra-small MoN nanoparticle with the size less than 10 nm. (c) High magnified TEM image reveals that the MoN nanoparticles are crystalline in nature where distinct fringes can be clearly observed.

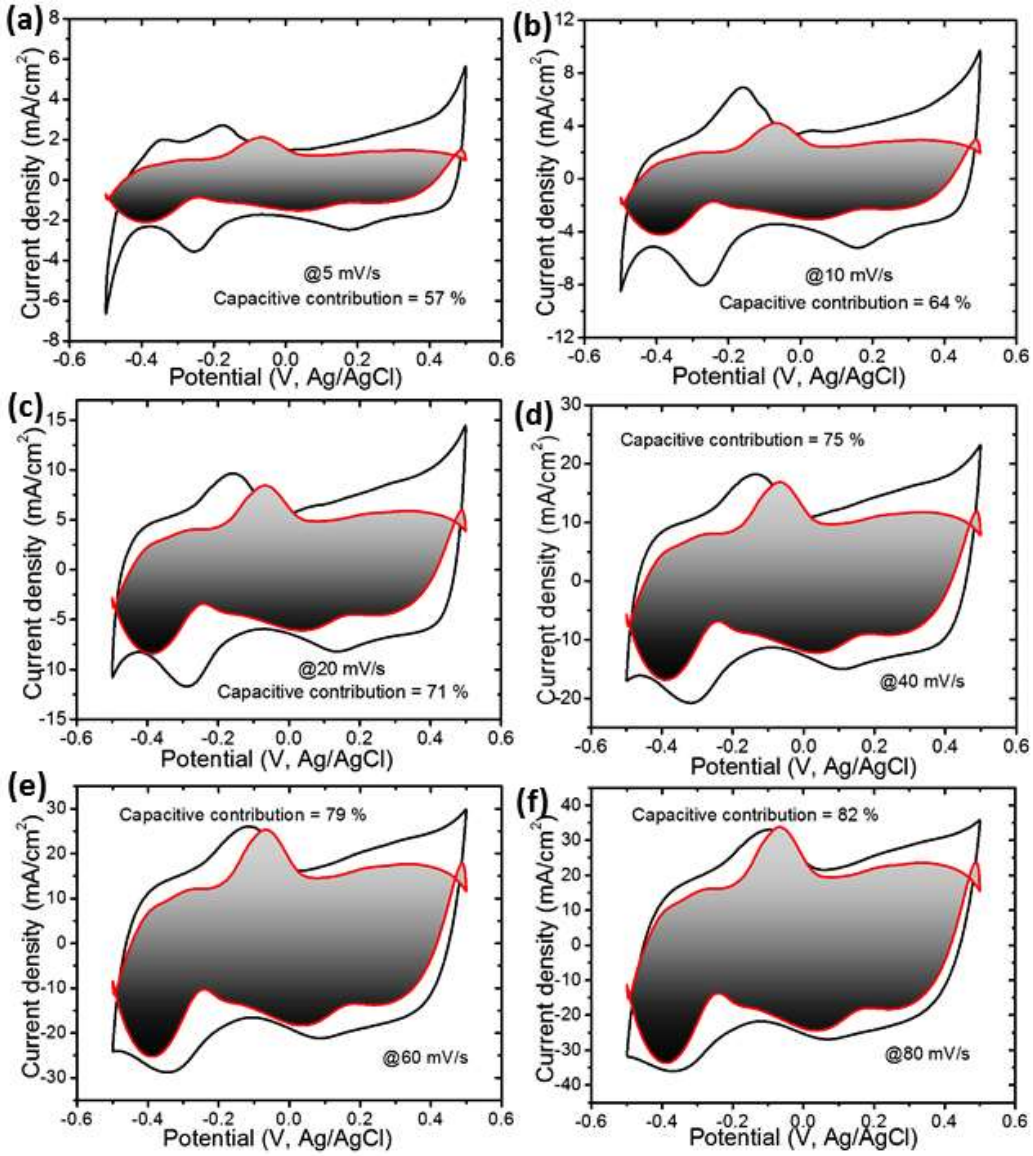


**Figure S3 Electrochemical characterization of MoN@P-CF samples, Related to Figure 3.** Cyclic voltammetry curves for MoN@P-CF-900 electrode at different scan rates from 10 to 100 mV/s. The capacitive contribution to the total current is shown by the shaded region.

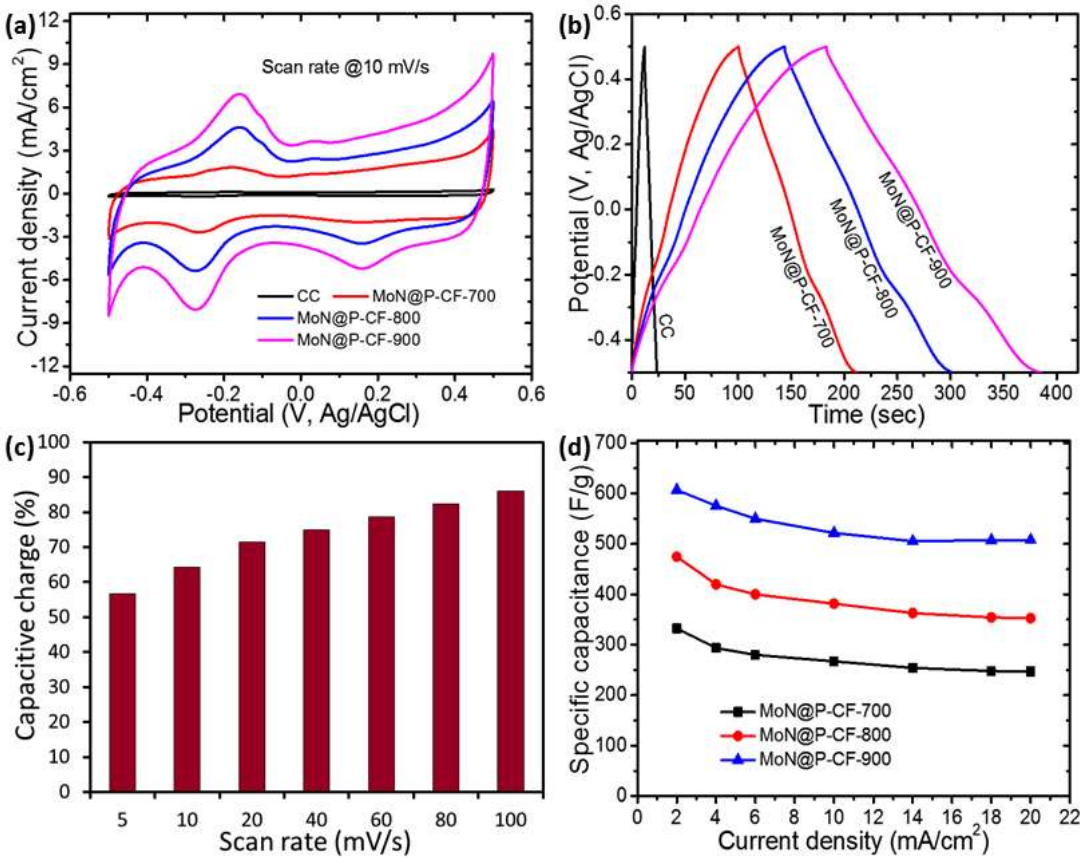


**Figure S4 Electrochemical characterization of MoN@P-CF samples, Related to Figure 3**. (a, b) Cyclic voltammetry and Galvanostatic CD curves recorded for MoN@P-CF samples prepared at different nitridation temperatures. (c) Variation of capacitive contribution with scan rate. (d) Variation of specific capacitance with current densities for different MoN@P-CF electrodes.

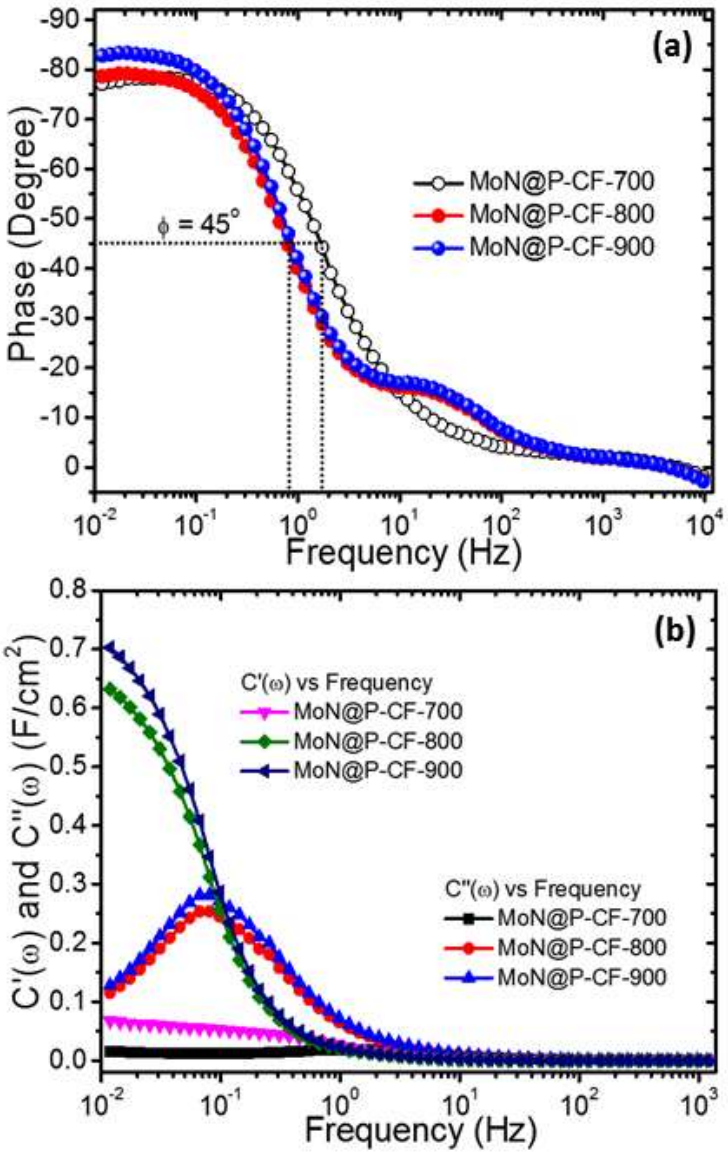


**Figure S5 Electrochemical characterization of MoN@P-CF samples, Related to Figure 3**. (a) Bode plots and (b) Real and imaginary capacitances with frequency for the MoN@P-CF samples prepared at different nitridation temperatures. The plot shows common relaxation-type dispersions where the real capacitance C' reduces with frequency while C'' shows maxima.

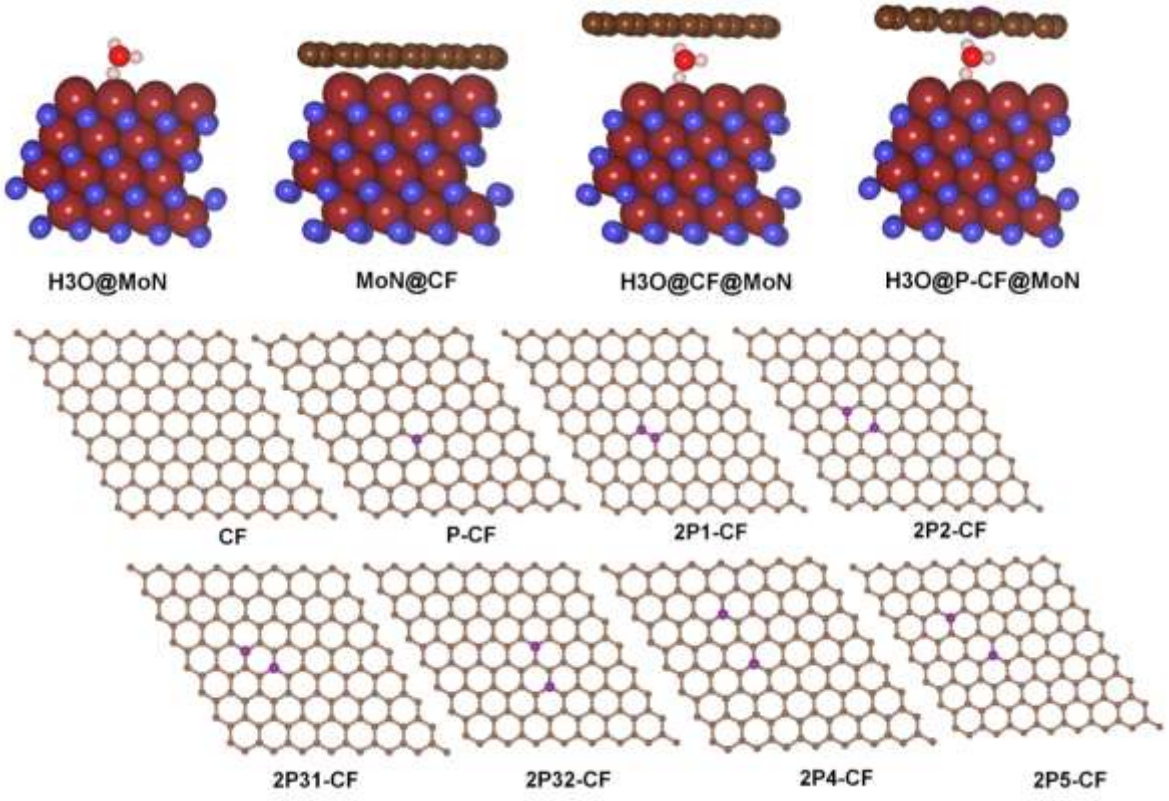


**Figure S6 Initial Models of our DFT simulations of H3O+ adsorption on CF, P-CF, MoN, MoN@CF, and MoN@P-CF systems, Related to Figure 4.** MoN, MoN@CF, MoN@P-CF, and H3O+ are represented by balls. Color code: MoN:plum, N:blue, C:brown, O:red, P:pink, and H:white. Isolated CF and P-CF models are shown in the lower panel and represented in balls and sticks. Different relative positions of the two phosphorus atoms (pink color spheres) are noted by Arabic numbers such as: P-CF, graphene sheet doped with one phosphorus, 2P1-CF is graphene doped by two phosphorus separated by one bond, 2P31-CF is graphene doped by two phosphorus and separated by two bonds and first configuration. The second Arabic letter after the phosphorus atom refers to the configuration numbers.

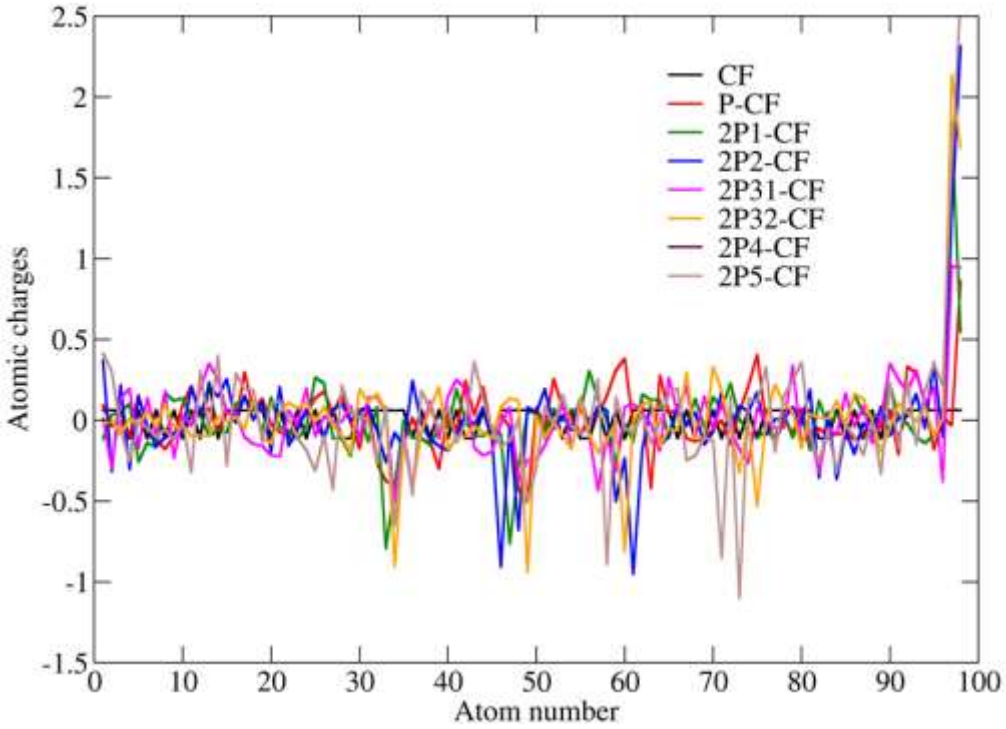


**Figure S7 AIM atomic charges are shown for all CF and P-CF models, Related to Figure 4**

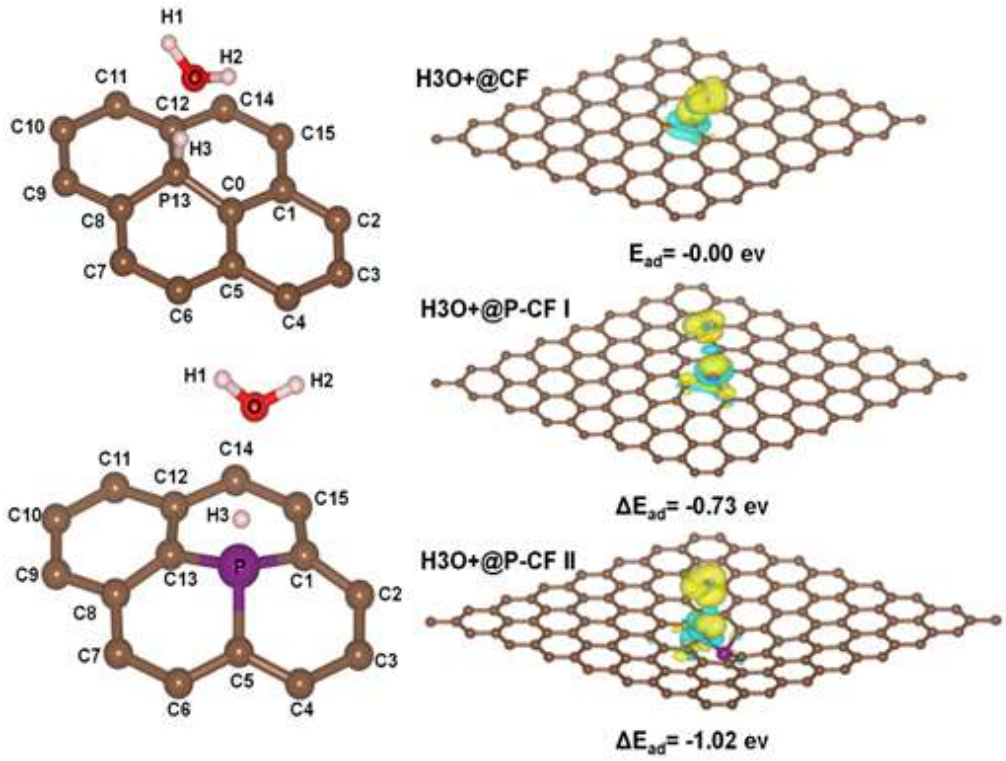


**Figure S8 Binding charge densities of $H3O^+$ on the pristine CF and P-CF in two different mode of adsorption**, **Related to Figure 4.** The isosurfaces is represented in resolution of 0.0025 electron/bohr3. Yellow is rich and blue is depletion of electron density. Left panel is showing the important carbon atoms surrounding the $H3O^+$ adsorption site in case of CF and P-CF I.

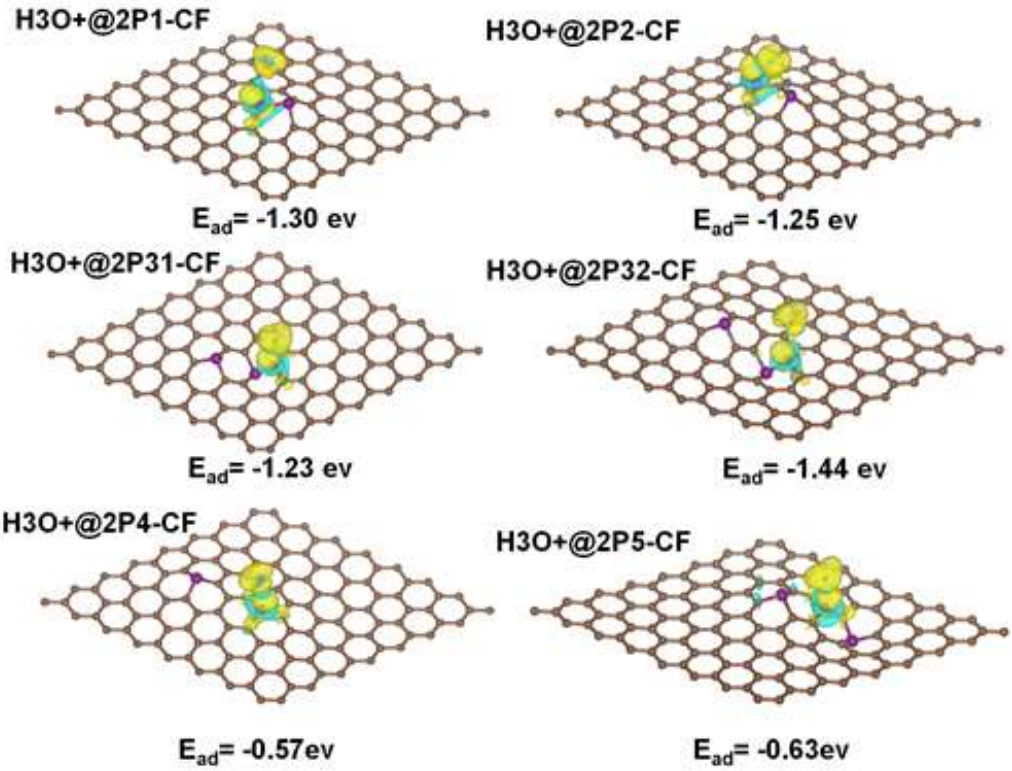


**Figure S9: Binding charge densities of H3O+ on P-CF models following the same nomenclature reported in Figure S6, Related to Figure 4.** The isosurfaces is represented in resolution of 0.015 electron/bohr3. Yellow is rich and blue is depletion of electron density.

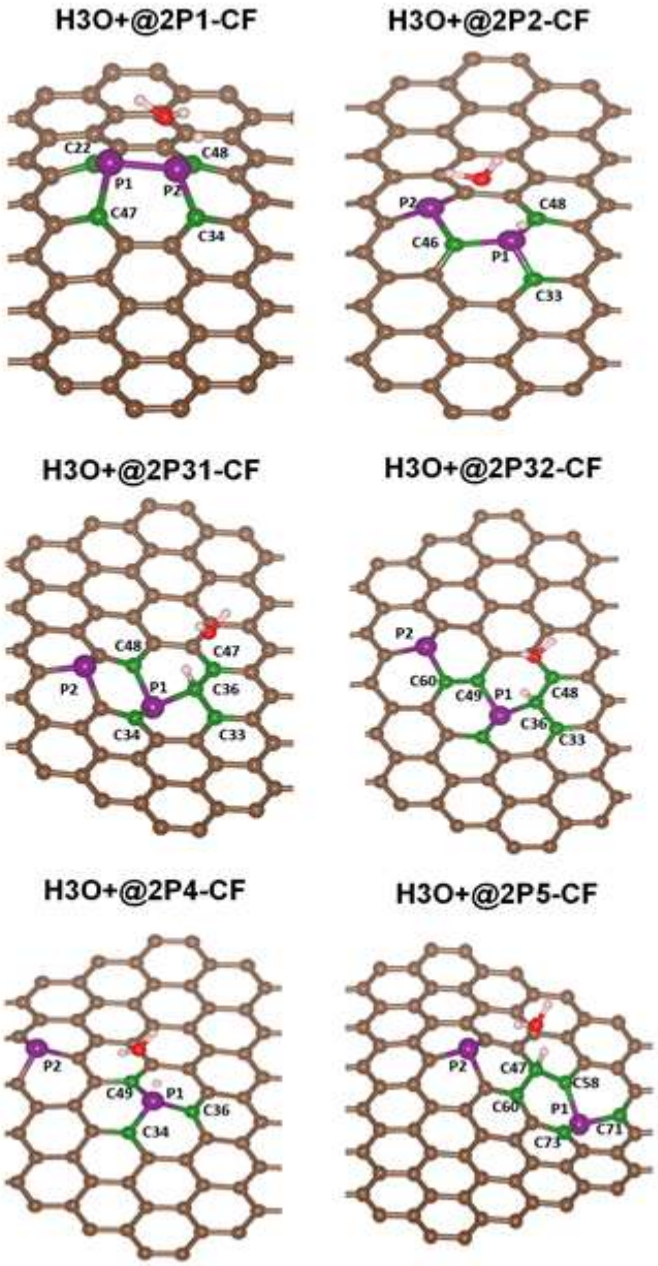


**Figure S10 H3O+ binding sites of the P-CF considered systems depicted in Figure S9, Related to Figure 4.** The important carbon atoms are colored in green the remaining is following the color code in Figure S6 and S9. The corresponding atomic charges are reported in Table S2.

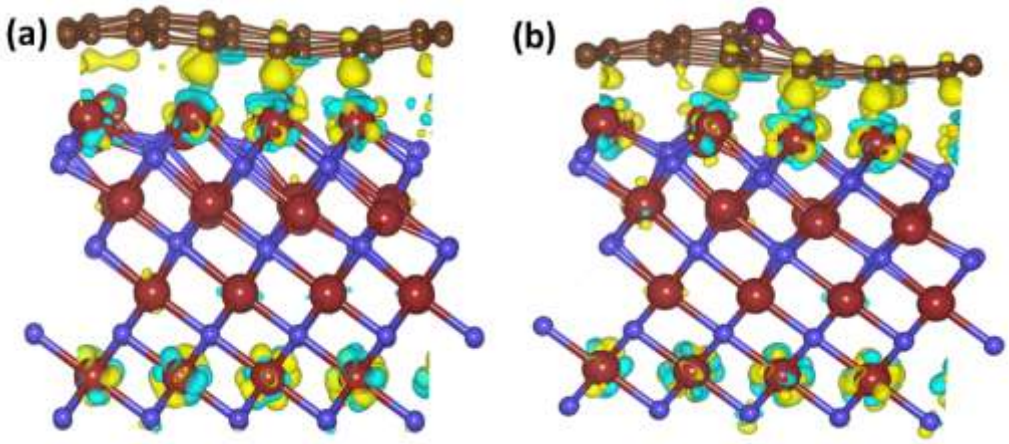


**Figure S11 Charge density difference between the nano-composite MoN@CF, and MoN@P-CF, and their fragments (isolated slab, CF, and P-CF sheets)**, **Related to Figure 4**. The isosurfaces is represented in resolution of 0.015 electron/bohr3. Yellow is rich and blue is depletion of electron density. Color code is the same as in Figure S6.

**$RuO_2$@CF: Film formation mechanism, Related to Figure 5.**

The deposition of $RuO_2$ on the surface of carbon fabric (CF) was carried out using Layer-by-Layer method (LBL) by immersing CF in separately placed cationic and anionic precursors with rinsing between every immersion. The growth kinetics of the deposition process is based on ion-by-ion deposition at nucleation sites on the immersed surfaces.

In present investigation, $RuO_2$ were grown on the surface of CF through a controlled heterogeneous precipitation of $RuCl_3$. The proposed reaction mechanism is as follows: thin layer of Ru-species are adsorbed on the CF-substrate by immersion of the CF into the cationic precursor solution kept at room temperature (10 mM $RuCl_3$).

$$RuCl_3 + 3H_2O \rightarrow Ru(OH)_3^+ + 3HCl \qquad (9)$$

With further reaction is followed by the immersion of the wet substrate in $H_2O_2$ anionic solution, where the chemical reaction between oxygen species and pre-adsorbed Ru-species leads to the formation of thin layer of $RuO_2$ on the surface of CF.

$$2Ru(OH)_3^+ + H_2O_2 \rightarrow 2RuO_2 + 4H_2O \qquad (10)$$

This completes one cycle of deposition of $RuO_2$ at CF. We have performed different number of deposition cycles to obtain desired mass loadings.

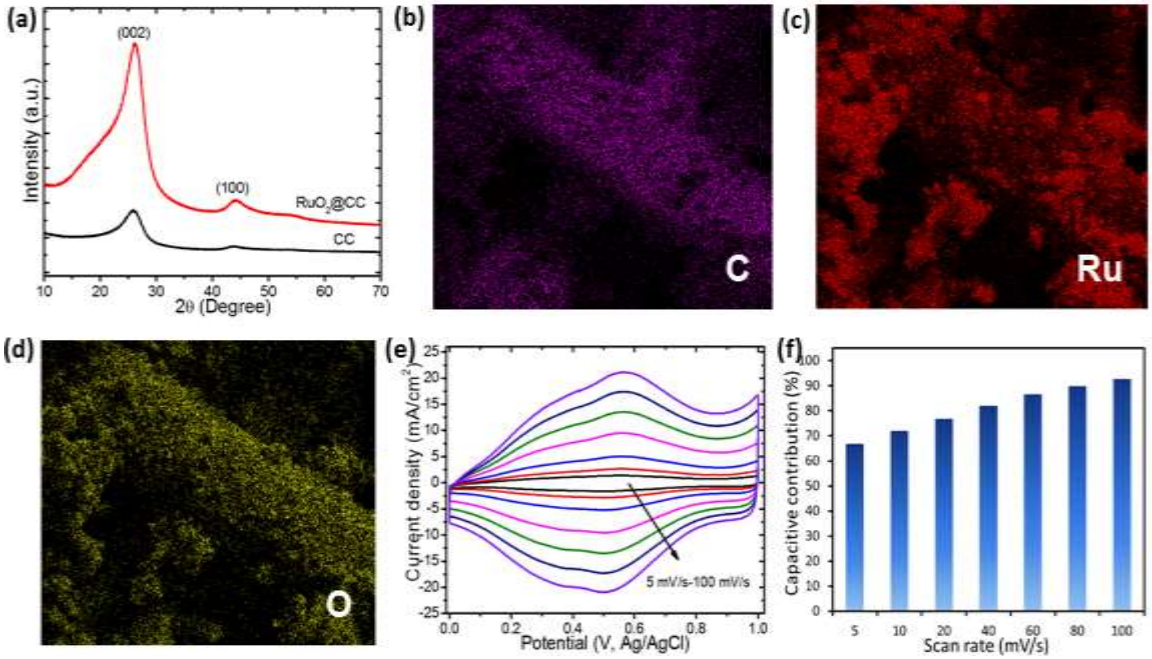


**Figure S12 Characterizations of $RuO_2$@CF, Related to Figure 5.** (a) XRD patterns of bare and $RuO_2$ coated carbon fabric electrodes. (b-d) EDS mapping images, displaying homogeneous coating of C, Ru and O, respectively. (e) CV curves measured at different scan rates in 1M $H_2SO_4$ electrolyte. (c) Plot of capacitive contribution as a function of scan rates.

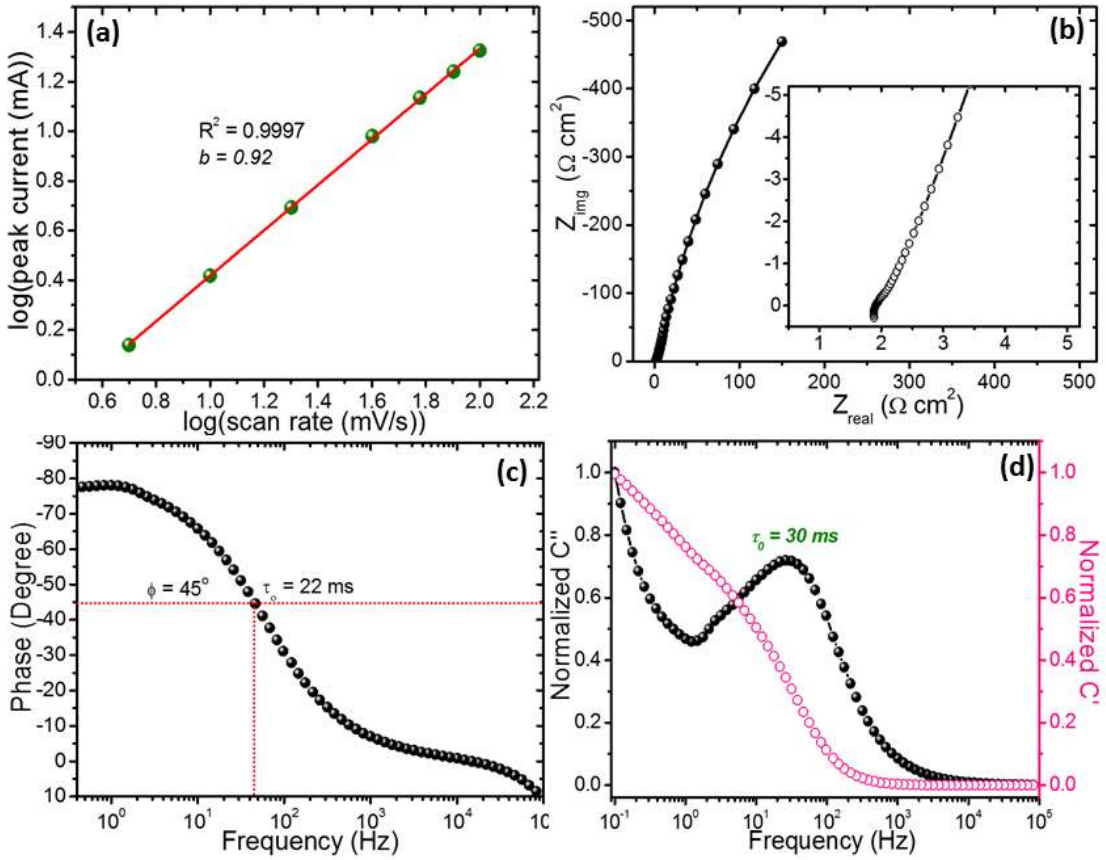


**Figure S13 Electrochemical characterizations of $RuO_2$@CF**, **Related to Figure 5**: (a) A plot of log (peak current, *i*) versus log(scan rate, mV/s), suggesting the major contribution to total current is from pseudocapacitive mechanism (b=0.92). (b) Nyquist plot recorded in the frequency range of 10 mHz to 100 kHz with amplitude of 5 mV. (c) Bode plots and (d) Real and imaginary capacitances with frequency, implying fast charge/discharge rates as relaxation time constant ($\tau_0 = 1/f_0$) was found to be 22-30 ms.

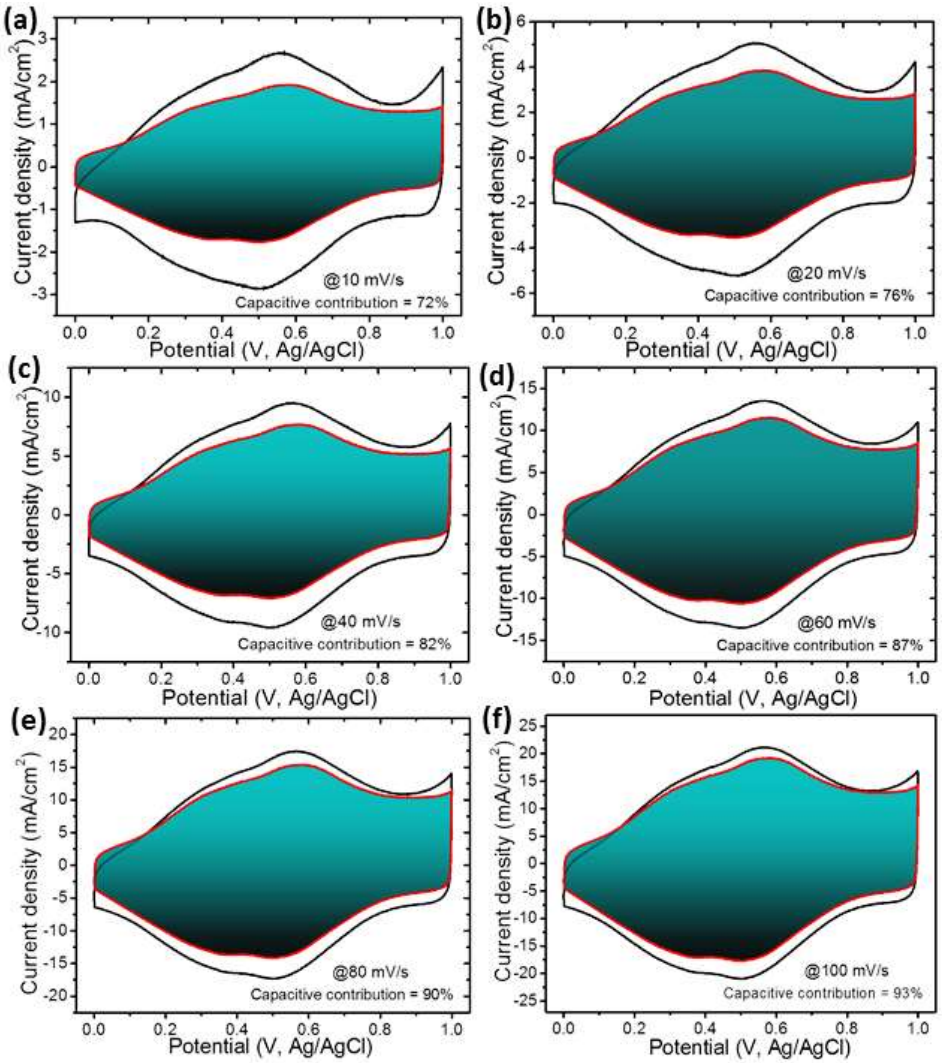


**Figure S14 Electrochemical characterization of $RuO_2$@CF, Related to Figure 5.** Cyclic voltammetry curves for $RuO_2$@CF electrode at different scan rates from 10 to 100 mV/s. The capacitive contribution to the total current is shown by the shaded region.

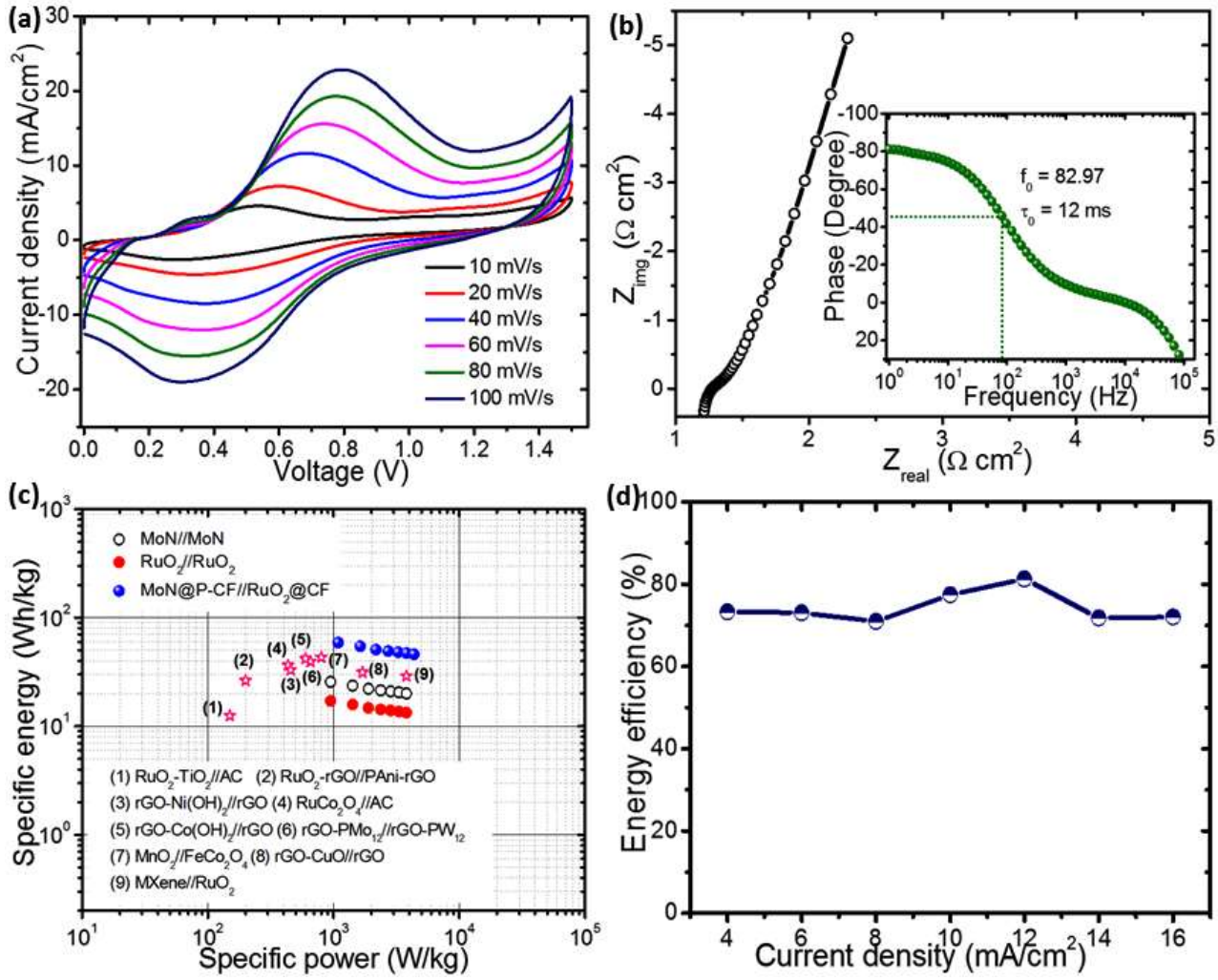


**Figure 15 Electrochemical characterization of MoN@P-CF//$RuO_2$@CF cell, Related to Figure 6.** (a) CV profiles for MoN@P-CF//$RuO_2$@CF asymmetric cell recorded at different scan rates. (b) Nyquist plot with their corresponding bode plot, confirming ultra-fast characteristics of the cell. (c) Ragone plot showing comparison of specific energy and specific power values with RuO2 based asymmetric systems. (d) Energy efficiency of device calculated at different current densities.

**Table S1 Electrochemical performances of nitrides based electrodes for supercapacitor application, Related to Figure 3**

| Material | Electrolyte | Capacitance | Ref. |
|---|---|---|---|
| MoN@P-CF | 1 M $H_2SO_4$ | 400 mF/cm$^2$ at 2 mA/cm$^2$ | Present work |
| Molybdenum Oxynitride | 1 M KOH | 736.6 mF/cm$^2$ at 10 mV/s | Ruan et al. 2017 |
| TiN | 0.5 M $H_2SO_4$ | 27.3 mF/cm$^2$ at a current density of 1.0 mA/cm$^2$ | Wei et al. 2018 |
| CrN | 0.5 M $H_2SO_4$ | 12.8 mF/cm$^2$ at 1.0 mA/cm$^2$ | Wei et al. 2017 |
| TiN | 0.5 M $K_2SO_4$ | 8.8 mF/cm$^2$ at 100 mV/s | Achour et al. 2015 |
| MoN | 1 M $H_2SO_4$ | 928 F/cm$^3$ at 2 mV/s | Xiao et al. 2017 |
| MoN | 1 M KOH | 130 mC/cm$^2$ at 2 mA/cm$^2$ | Nandi et al. 2018 |
| TiN | 1 M $H_2SO_4$ | 10.9 mF/cm$^2$ at 0.1 V/s | Zheng et al. 2018 |
| $MoN_x$/TiN | 1 M LiOH | 121.50 mF/cm$^2$ for at 0.3 mA/cm$^2$ | Xie et al. 2017 |
| $Mo_2N$ | 1 M $H_2SO_4$ | 172 F/g at 1 mV/s | Xue-liang et al. 2009 |
| $Mo_XN$ | 4.4 M $H_2SO_4$ | 315 F/cm$^3$ at 10 mV/s | Roberson et al. 1999 |
| $Mo_2N$ | 1 M $H_2SO_4$ | 171 F/g at 0.5 mA/cm$^2$ | Zhang et al. 2016 |
| $Mo_3N_2$ | 1 M KOH | 220 F/g at 50 mV/s | Lee et al. 2013 |
| $Mo_2N$ | 0.5 $Li_2SO_4$ | 722 F/cm$^3$ at 5 mV/s | Chen et al. 2017 |
| $Mo_2N$ | 0.5 M $K_2SO_4$ | 275 F/g | Shah et al. 2014 |
| $Mo_2N$@C-rGO | 1 M $H_2SO_4$ | 514.54 F/g at 0.25 A/g | Sridhar et al. 2018 |
| TiN@$MoS_2$ | 0.5 M $H_2SO_4$ | 662.2 mF/cm$^2$ at 1 mA/cm$^2$ | Yu et al. 2017 |

**Table S2 $H3O^+$ adsorption energies are reported referenced to the adsorption energy of CF pristine sheet. All energies are reported in electron volt (ev), Related to Figure 4.**

| Model | $\Delta E_{ads}$ |
|---|---|
| CF | 0.0 |
| P-CF | -1.02 |
| 2P1-CF | -1.30 |
| 2P2-CF | -1.25 |
| 2P31-CF | -1.23 |
| 2P32-CF | -1.44 |
| 2P4-CF | -0.57 |
| 2P5-CF | -0.63 |
| MoN | -5.77 |
| MoN@CF | -8.20 |
| MoN@CF-P | -8.47 |

**Table S3 Atomic charges are reported for H3O+ adsorption site in the three molecular models shown in Figure S7, Related to Figure 4**

| Atom | CF | P-CF I | P-CF II |
|---|---|---|---|
| C1 | -0.028 | -0.313 | -0.414 |
| C2 | 0.009 | -0.073 | 0.002 |
| C3 | -0.082 | 0.171 | 0.062 |
| C4 | 0.226 | -0.114 | -0.025 |
| C5 | 0.172 | -0.335 | -0.439 |
| C6 | -0.150 | -0.107 | 0.126 |
| C7 | -0.217 | 0.116 | -0.057 |
| C8 | 0.087 | -0.013 | 0.139 |
| C9 | 0.035 | 0.081 | -0.044 |
| C10 | 0.047 | 0.077 | -0.142 |
| C11 | 0.110 | 0.104 | 0.024 |
| C12 | 0.194 | -0.017 | 0.190 |
| C13 | -0.025 | -0.294 | -0.378 |
| C14 | -0.164 | 0.023 | -0.091 |
| C15 | -0.270 | -0.124 | 0.087 |
| C0 | 0.0272 | NA | NA |
| P | NA | 1.125 | 1.121 |
| O | -1.0396 | -0.9587 | -1.0241 |
| H1 | 0.5356 | 0.5014 | 0.5365 |
| H2 | 0.5562 | 0.5178 | 0.5320 |
| H3 | 0.0589 | -0.1945 | 0.0465 |

**Table S4 Atomic charges are reported for complexes of H3O+ adsorbed on P-CF systems as depicted in Figure S9, Related to Figure 4 (Provided in Separate Excel sheet)**

**$H_3O_+$ adsorption on P-doped CF at 2%.**

**Results shown in S9, 10 and Table S4 can be explained based on the atomic charges reported in table S4 (excel sheet).** The adsorption of $H_3O^+$ on 2P-CF fibers can be classified into two groups; the first group that display negative charges on the adsorbed proton as well as on adsorption site atoms (2P1-CF, 2P2-CF, and 2P4-CF) and the binding site is on P atoms. The second group has positive charge on the adsorbed proton and negative on the surrounding atoms (2P31-CF, 2P32-CF and 2P5-CF). The adsorption site of the latter group is on C atoms. In the first group, the repulsion between the adsorbed protons and the surrounding atoms decreases their stabilities, while the attractive forces induced by the positive charges on P atoms and the adsorbed proton balanced them. Their affinity is dependent on the distance between the two phosphorus atoms. In the second group, the situation is reversed, the attractive electrostatic forces between the adsorbed protons and the binding site atoms increased their stabilities while the repulsive forces with the positive charges on P atoms decrease them. The affinity of this group is also dependent on the distance between the binding site and the two P atoms.

**Table S5 AIM atomic charges are reported for the complexes of H3O+ adsorbed on MoN, MoN@CF, and MoN@P-CF depicted in Figure S8. Related to Figure 4 (Provided in Separate Excel sheet)**

**Table S6 Comparison of electrochemical performances of MoN@P-CF//$RuO_2$@CF asymmetric supercapacitor cell, Related to Figure 6**

| Material used | Type of cell | Capacitance | Maximum Energy density | Maximum Power density | Stability | Ref. |
|---|---|---|---|---|---|---|
| MoN@P-CF//$RuO_2$@CF | Asymmetric cell | 7.74 F/$cm^3$ at 4 mA/$cm^2$ | 2.4 mWh/$cm^3$ | 174 mW/$cm^3$ | 89 % over 15000 cycles | **Present work** |
| VOx//VN | Asymmetric cell | 1.01 F/$cm^3$ (44.9 F/g) at 0.5 mA/$cm^2$ | 0.61 mWh/$cm^3$ at 0.5 mA/$cm^2$ | 0.85 W/$cm^3$ at 5 mA/$cm^2$ | 87.5 % over 10000 cycles | Lu et al. 2013 |
| TiN@GNS//$Fe_2$N@GNS | Asymmetric cell | 60 F/g at 4 A/g | 0.51 mWh/$cm^3$ at 2 A/g | 422.7 mW/$cm^3$ at 16 A/g | 99.8% over 20000 cycles | Zhu et al. 2015 |
| TiN/TiN | Symmetric cell | 0.33 F/$cm^3$ at 2.5 mA/$cm^3$ | 0.05 mWh/$cm^3$ at 2.5 mA/$cm^3$ | - | 82 % over 15000 cycles | Lu et al. 2012 |
| $Mo_2$N@rGO/ $Mo_2$N@rGO | Symmetric cell | 15.4 F/$cm^3$ at 0.1 A/$cm^3$ | 1.05 mWh/$cm^3$ at 0.1 A/$cm^3$ | 3.15 W/$cm^3$ at 2 A/$cm^3$ | 85.7% over 4000 cycles | Ma et al. 2015 |
| PANI//C/$Mo_x$N | asymmetric cell | 65.2 F/g at 0.5 A/g | 14.1 Wh/kg at 0.5 A/g | - | 40.8 % over 3000 cycles | Tan et al. 2018 |
| $MnO_2$/GNS// $MoS_2$/GNS | asymmetric cell | 142 F/g (415 mF/$cm^2$ and 19.3 F/$cm^3$) at 2 mV/s | 230.8 mWh/ $cm^2$ at | 5.0 kW/kg | 90 % over 5000 cycles | Yang et al. 2016 |
| NiS/$MoS_2$//AC | asymmetric cell | 108 F/g at 0.5 A/g | 40 Wh/kg at 0.5 A/g | 16.8 W/kg at 20 A/g | 100 % over 10000 cycles | Yang et al. 2017b |
| $MoS_2$-NiO//$MoS_2$-$Fe_2O_3$ | Asymmetric cell | - | 39.6 Wh/kg at 1 A/g | - | 95 % over 6000 cycles | Wang et al. 2017 |
| $RuO_2$//$Fe_2O_3$ | Asymmetric cell | 54.5 mF/$cm^2$ at 0.13 mA/$cm^2$ | 1.5 mWh/ $cm^3$ at 0.13 mA/$cm^2$ | - | 97 % over 5000 cycles | Wang et al. 2018 |

**Supplemental References**


Achour, A., Porto, R., Soussou, M., Islam, M., Boujtit, M., Aissa, K., Brizoual, L., Djouadi, A., Brousse, T. (2015). Titanium nitride films for micro-supercapacitors: Effect of surface chemistry and film morphology on the capacitance J. Power Sources 300, 525-532.

Blochl. P. E. (1994). Projector augmented-wave method. Phys. Rev. B, 50, 17953.

Bull, C. L., McMillan, P. F., Soignard, E., Leinenweber, K. (2004) Determination of the crystal structure of δ-MoN by neutron diffraction. J. Solid State Chem., *177*, 1488–1492

Chen, L., Liu, C., Zhang, Z. (2017). Novel [111] oriented γ-$Mo_2N$ thin films deposited by magnetron sputtering as an anode for aqueous micro-supercapacitors. Electrochimica Acta 245, 237–248.

Dudarev, S. L., Botton, G. A., Savrasov, S. Y., Humphreys, C. J., Sutton, A. P. (1998). Electron-energy-loss spectra and the structural stability of nickel oxide:An LSDA1U study. Phys. Rev. B 57, 1505–1509.

Grimme, S., Antony, J., Ehrlich, S., Krieg, H. (2010). A consistent and accurate ab initio parametrization of density functional dispersion correction (DFT–D) for the 94 elements H–Pu. J. Chem. Phys. 132, 154104.

Kresse, G., Hafner, J. (1993). Ab initio molecular dynamics for liquid metals. Phys. Rev. B, 47, 558

Kresse, G., Hafner, J. (1994). Ab initio molecular-dynamics simulation of the liquid-metal-amorphous-semiconductor transition in germanium. Phys. Rev. B, 49, 14251.

Lee, K., Lee, Y., Ko, A., Cao, G., Park, K. (2013). Single-crystalline mesoporous molybdenum nitride nanowires with improved electrochemical properties. J. Am. Ceram. Soc., 96, 37–39.

Lu, X., Wang, G., Zhai, T., Yu, M., Xie, S., Ling, Y., Liang, C., Tong, Y., Li, Y. (2012). Stabilized TiN nanowire arrays for high-performance and flexible supercapacitors. Nano Lett. 12, 5376−5381.

Lu, X., Yu, M., Zhai, T., Wang, G., Xie, S., Liu, T., Liang, C., Tong, Y., Li, Y. (2013) High energy density asymmetric quasi-solid-state supercapacitor based on porous vanadium nitride nanowire anode. Nano Lett. 13, 2628-2633.

Monkhorst, H., Pack, J. (1976). Special points for Brillouin–zone integrations. Phys. Rev. B 13, 5188-5192.

Momma, K., Izumi, F. (2011). VESTA 3 for three-dimensional visualization of crystal, volumetric and morphology data. J. Appl. Crystallogr., 44**,** 1272-1276.

Ma, G., Wang, Z., Gao, B., Ding, T., Zhong, Q., Peng, X., Su, J., Hu, B., Yuan, L., Chu, P., Zhou, J., Huo, K. (2015). Multilayered paper-like electrodes composed of alternating stacked mesoporous Mo2N nanobelts and reduced graphene oxide for flexible all-solid-state supercapacitors. J. Mater. Chem. A, 3, 14617–14624.

Nandi, D. K., Sahoo, S., Kim, T. H., Cheon, T., Sinha, S., Rahul, R., Jang, Y., Bae, J., Heo, J., Shim, J., Kim, S. (2018). Low temperature atomic layer deposited molybdenum nitride-Ni-foam composite: An electrode for efficient charge storage. Electrochem. Commun. 93, 114–118.

Perdew, J. P., Burke, K. , Ernzerhof, M. (1996) Generalized gradient approximation made simple. Phys. Rev. Lett., 77, 3865.

Perdew, J. P., Burke, K. , Ernzerhof, M. (1997) Erratum: Generalized gradient approximation made simple. Phys. Rev. Lett., 78, 1396.

Ruan, D., Lin, R., Jiang, K., Yu, X., Zhu, Y., Fu, Y., Wang, Z., Yan, H., Mai, W. (2017). High-Performance Porous Molybdenum Oxynitride Based Fiber Supercapacitors. ACS Appl. Mater. Interfaces, 9, 29699-29706.

Roberson, S. L., Finello, D., Davis, R. F. (1999). Electrochemical evaluation of molybdenum nitride electrodes in H2SO4 electrolyte. J. Appl. Electrochem., 29, 75-80.

Shah, S., Hector, A., Owen, J., (2014). Redox supercapacitor performance of nanocrystalline molybdenum nitrides obtained by ammonolysis of chloride-and amide-derived precursors. J. Power Sources 266, 456-463.

Sridhar, V., Park, H. (2018). Carbon sheathed molybdenum nitride nanoparticles anchored on reduced graphene oxide as high-capacity sodium-ion battery anodes and supercapacitors. New J. Chem., 42, 5668-5673.

Tan, Y., Meng, L., Wang, Y., Dong, W., Kong, L., Kang, L., Ran, F. (2018). Negative electrode materials of molybdenum nitride/N-doped carbon nano-fiber via electrospinning method for high-performance supercapacitors. Electrochimica Acta 277, 41-49.

Wei, B., Liang, H., Zhang, D., Qi, Z., Shen, H., Wang, Z. (2018). Magnetron sputtered TiN thin films toward enhanced performance supercapacitor electrodes. Mater Renew Sustain Energy 7, 11.

Wei, B., Liang, H., Zhang, D., Wu, Z., Qi, Z., Wang, Z. (2017). CrN thin films prepared by reactive DC magnetron sputtering for symmetric supercapacitors. J. Mater. Chem. A 5, 2844-2851.

Wang, K., Yang, J., Zhu, J., Li, L., Liu, Y., Zhang, C., Liu, T. (2017) General solution-processed formation of porous transition-metal oxides on exfoliated molybdenum disulfides for high-performance asymmetric supercapacitors. J. Mater. Chem. A, 5, 11236-11245.

Wang, Q., Liang, X., Ma, Y., Zhang, D. (2018). Fabrication of hollow nanorod electrodes based on RuO2//Fe 2 O 3 for an asymmetric supercapacitor. Dalton Trans., 47, 7747–7753.

Xie, Y., Tian, F. (2017). Capacitive performance of molybdenum nitride/titanium nitride nanotube array for supercapacitor. Mater. Sci. Eng. B 215, 64–70

Xue-liang, L., Yan, X., Hua, W., Hua-lin, W., Wei-dong, W., Xiang-ying, C. (2009) Synthesis and characterization of uniform nanoparticles of γ-Mo2N for supercapacitors. Trans. Nonferrous Met. Soc. China 19, 620-625.

Xiao, X., Yu, H., Jin, H., Wu, M., Fang, Y., Sun, J., Hu, Z., Li, T., Wu, J., Huang, L., Gogotsi, Y., Zhou, J. (2017). Salt-Templated Synthesis of 2D Metallic MoN and Other Nitrides. ACS Nano 11, 2180-2186.

Yang, X., Niu, H., Jiang, H., Wang, Q., Qu, F. (2016). A high energy density all-solid-state asymmetric supercapacitor based on MoS2/graphene nanosheets and MnO2/graphene hybrid electrodes. J. Mater. Chem. A, 4, 11264–11275.

Yang, N., Zheng, X., Li, L., Li, J., Wei, Z., (2017). Influence of Phosphorus Configuration on Electronic Structure and Oxygen Reduction Reactions of Phosphorus-Doped Graphene, J. Phys. Chem. C, 121, 19321-19328.

Yang, X., Zhao, L., Lian, J. (2017). Arrays of hierarchical nickel sulfides/Mo2 nanosheets supported on carbon nanotubes backbone as advanced anode materials for asymmetric supercapacitor. J. Power Sources 343, 373-382.

Yu, M., Trinkle, D. R. (2011) Accurate and efficient algorithm for Bader charge integration, J. Chem. Phys. 134, 064111.

Yu, M., Zhao, S., Feng, H., Hu, L., Zhang, X., Zeng, Y., Tong, Y., Lu, X. (2017). Engineering Thin $MoS_2$ Nanosheets on TiN Nanorods: Advanced Electrochemical Capacitor Electrode and Hydrogen Evolution Electrocatalyst. ACS Energy Lett. 2, 1862−1868.

Zhang, W., Ma, X., Kong, L., Liu, M., Luo, Y., Kang, L. (2016). Electrochemical performance of pseudo-capacitive intermetallic molybdenum nitride in acid. J. Electrochem. Soc., 163, A1300-A1305.

Zheng, T., Tahmasebi, M., Li, B., Li, Y., Ran, S., Glen, T., Lam, K., Choi, I., Boles, S. (2018). Sputtered Titanium Nitride Films on Titanium Foam Substrates as Electrodes for High-Power Electrochemical Capacitors. ChemElectroChem 5, 2199-2207.

Zhu, C., Yang, P., Chao, D., Wang, X., Zhang, X., Chen, S., Tay, B., Huang, H., Zhang, H., Mai, W., Fan, H. (2015). All Metal Nitrides Solid-State Asymmetric Supercapacitors. Adv. Mater., 27, 4566–4571.